

# Extra adsorption and adsorbate superlattice formation in metal–organic frameworks

Hae Sung Cho<sup>1\*</sup>, Hexiang Deng<sup>2,3\*</sup>, Keiichi Miyasaka<sup>1\*</sup>, Zhiyue Dong<sup>2</sup>, Minhyung Cho<sup>1</sup>, Alexander V. Neimark<sup>4</sup>, Jeung Ku Kang<sup>1</sup>, Omar M. Yaghi<sup>1,5,6</sup> & Osamu Terasaki<sup>1,7</sup>

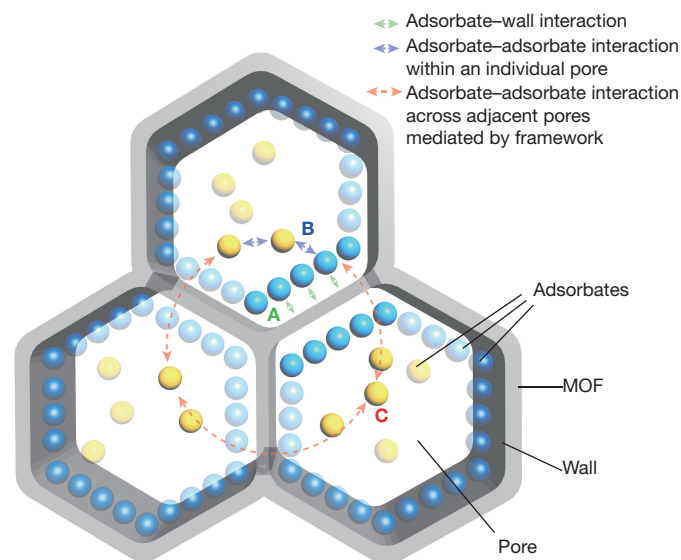
**Metal-organic frameworks (MOFs) have a high internal surface area and widely tunable composition<sup>1,2</sup>, which make them useful for applications involving adsorption, such as hydrogen, methane or carbon dioxide storage<sup>3–9</sup>. The selectivity and uptake capacity of the adsorption process are determined by interactions involving the adsorbates and their porous host materials. But, although the interactions of adsorbate molecules with the internal MOF surface<sup>10–17</sup> and also amongst themselves within individual pores<sup>18–22</sup> have been extensively studied, adsorbate–adsorbate interactions across pore walls have not been explored. Here we show that local strain in the MOF, induced by pore filling, can give rise to collective and long-range adsorbate–adsorbate interactions and the formation of adsorbate superlattices that extend beyond an original MOF unit cell. Specifically, we use *in situ* small-angle X-ray scattering to track and map the distribution and ordering of adsorbate molecules in five members of the mesoporous MOF-74 series along entire adsorption–desorption isotherms. We find in all cases that the capillary condensation that fills the pores gives rise to the formation of ‘extra adsorption domains’—that is, domains spanning several neighbouring pores, which have a higher adsorbate density than non-domain pores. In the case of one MOF, IRMOF-74-V-hex, these domains form a superlattice structure that is difficult to reconcile with the prevailing view of pore-filling as a stochastic process. The visualization of the adsorption process provided by our data, with clear evidence for initial adsorbate aggregation in distinct domains and ordering before an even distribution is finally reached, should help to improve our understanding of this process and may thereby improve our ability to exploit it practically.**

Figure 1 shows the three distinct types of interaction in which adsorbates in MOFs can engage: adsorbate molecules can interact with the material's internal surface (regime A); adsorbates can interact among themselves within the confines of a pore (regime B); and adsorbates can interact with each other across pores mediated by the material framework (regime C). Studying the collective adsorbate behaviour in regimes B and C requires porous MOF crystals, with pores that are large enough to enable the organization and behaviour of confined adsorbates to be observed, and with pore walls that are atomically thin and well-defined so as to allow observation of any local perturbations resulting from adsorption. In such systems, we can then use *in situ* small-angle X-ray scattering (SAXS) to detect long-range ordering of adsorbates in multiple pores at precisely controlled temperatures and pressures.

We chose the five mesoporous MOFs with isorecticular structure (IRMOF-74-III, IRMOF-74-IV, IRMOF-74-V, IRMOF-74-V-hex and IRMOF-74-VII) that are based on the crystalline IRMOF-74

structure<sup>8,23–25</sup>. The robustness of the IRMOF-74 honeycomb-like structure (in projection) is imparted by one-dimensional, rod-shaped magnesium oxide units that run along the pore direction and are held together by organic linkers (Fig. 2a). This rigid oxide unit allows for structural refinements in two dimensions, by keeping constant the structure along the *c* axis of the original MOF structure<sup>8</sup> (Fig. 2b). Thus, we apply the projected symmetry of the two-dimensional space groups (plane groups) *p3* or *p6* for the unit cell (Fig. 2b, green parallelogram). We therefore need only two variables, *h* and *k*, to specify the reflections with the *h* and *k* indices for the refinement. This allows us to focus on the adsorption region, and stops us from having to deal unnecessarily with the more complicated original symmetry *R3* in IRMOF-74-IV, IRMOF-74-V and IRMOF-74-VII, or *R3̄* in IRMOF-74-III and IRMOF-74-V-hex (Fig. 2b, red parallelogram).

All of these MOFs exhibit open porosity and have mesopores with sizes of 22 Å, 28 Å, 35 Å and 49 Å (for IRMOF-74-III, IRMOF-74-IV, IRMOF-74-V and IRMOF-74-VII, respectively). IRMOF-74-V-hex, having a pore size of 34 Å, was constructed with a linker functionalized



**Figure 1 | Three adsorbate-interaction regimes in mesoporous MOFs.** In regime A, adsorbed molecules interact (green arrows) with pore walls. In regime B, adsorbates interact amongst each other (blue arrows) within a pore. These two types of interaction and the corresponding regimes have been well studied. Regime C, however, has not been explored; here, adsorbates interact with each other (red arrows) across pore walls, in a way that is mediated by the framework. Light blue, molecules adsorbed onto the internal pore surface; yellow, molecules in the centre of the pores.

<sup>1</sup>Graduate School of Energy, Environment, Water and Sustainability, WCU/BK21Plus, KAIST, Daejeon 305-701, South Korea. <sup>2</sup>Key Laboratory of Biomedical Polymers-Ministry of Education, College of Chemistry and Molecular Sciences, Wuhan University, Luojiaoshan, Wuhan 430072, China. <sup>3</sup>The Institute for Advanced Studies, Wuhan University, Wuhan 430072, China. <sup>4</sup>Department of Chemical and Biochemical Engineering, Rutgers University, 98 Brett Road, Piscataway, New Jersey 08854, USA. <sup>5</sup>Department of Chemistry, University of California, Materials Sciences Division at Lawrence Berkeley National Laboratory, and Kavli Energy NanoSciences Institute, Berkeley, California 94720, USA. <sup>6</sup>King Fahd University of Petroleum and Minerals, Dhahran 34464, Saudi Arabia. <sup>7</sup>Department of Materials and Environmental Chemistry, Berzelii Centre EXSELENT on Porous Materials, Stockholm University, Stockholm SE-10691, Sweden.

\*These authors contributed equally to this work.

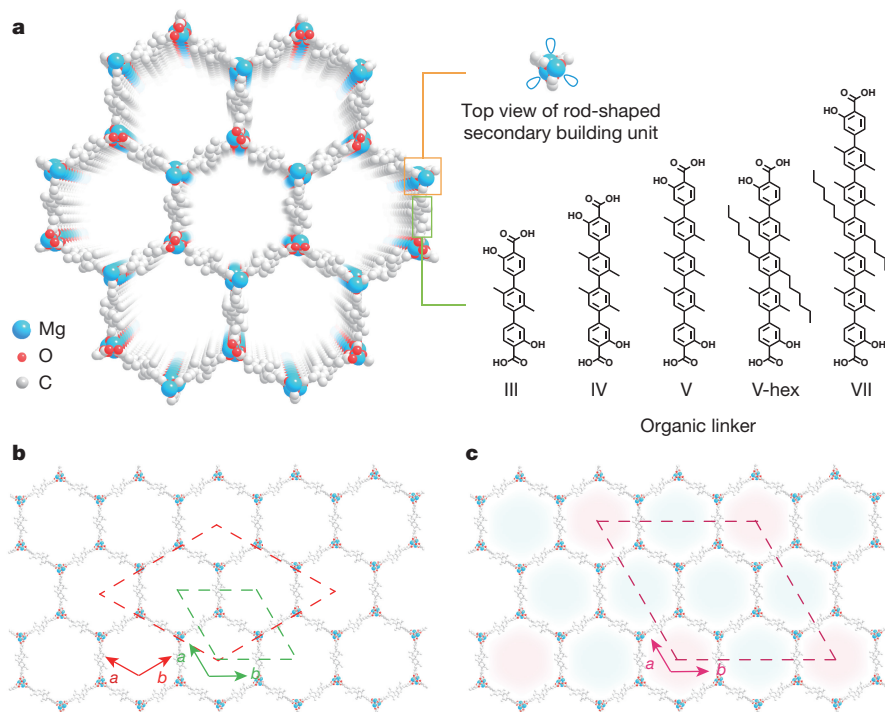


**Figure 2 | Structure of the IRMOF-74 series in three and two dimensions.** **a**, The honeycomb-like structure (in projection) of MOFs of the IRMOF-74 series is imparted by one-dimensional, rod-shaped magnesium oxide secondary building units, held together by organic linkers (III, IV, V, V-hex or VII). **b**, Green dashes show the two-dimensional unit cell, corresponding to plane groups  $p3$  and  $p6$ , that we

with a hexyl chain (V-hex). The atomically thin walls of the pores in these MOFs and their large pore sizes are key factors in their suitability for examining the collective behaviour of the adsorbates within and across the pores (regimes B and C, Fig. 1).

In contrast to other *in situ* adsorption studies, performed using a synchrotron beamline<sup>16,17,26</sup>, we used a laboratory-designed SAXS set-up operating in transmission mode with a rotating anode X-ray source, a graded confocal optic, and a Kratky block system to create a monochromatic beam focusing on the detector. Incorporation of an adsorption apparatus in the SAXS system enables measurement of both X-ray-diffraction profiles and gas-adsorption isotherms from the same sample at a precisely controlled temperature and adsorbate pressure (see Supplementary Information, section 1). We illustrate SAXS-based adsorption tracking for argon uptake by IRMOF-74-V-hex, for which the adsorption process can be divided into stages 1 to 5, taking place within the pressure ranges 0 to 0.5 kPa, 0.5 to 27 kPa, 27 to 33 kPa, 33 to 50 kPa and 50 to 100 kPa, respectively (Fig. 3a). Although the shape of the isotherm is similar to that of a type IV isotherm (as classified by the International Union of Pure and Applied Chemistry), typical for mesoporous materials, the distinct slopes seen in stages 4 and 5 point to two major differences. To understand the origin of slopes, we measured SAXS profiles along the entire adsorption curve, among which 11 different gas pressures (Fig. 3a) were selected to represent the different stages of the argon adsorption process (Fig. 3b).

The electron distribution of argon atoms introduced into the pores was obtained from 54 (7 independent) reflections, using difference Fourier analysis of the measured intensity profile of the argon-filled MOF and the calculated intensity profile of the corresponding activated MOF without argon (Fig. 3d; see also Supplementary Figs 4 and 5 and Tables 1–4). (Note that, although we cannot determine the argon distribution with atomic resolution owing to limitations imposed by the maximum  $q$  range (the largest angle that can be detected;  $4\pi\sin\theta/\lambda$ ) of the SAXS instrument, the resolution is sufficient to map the electron-distribution trend within the large pores;

applied for structural refinement. Red dashes shown the  $\sqrt{3} \times \sqrt{3}$  unit cell, which corresponds to the projection of the original space groups  $R3$  and  $R\bar{3}$ , used to reveal adsorbate distribution. **c**, The  $2 \times 2$  superlattice cell (purple dashes) and the pores in violet contain a larger number of adsorbates, compared with the surrounding pores in blue.

an exception is the centre point, which might be slightly affected by the termination effect in the Fourier synthesis.) The adsorbate electron-distribution maps (Fig. 3d) reveal that, as expected and in agreement with previous findings<sup>10</sup>, argon interacts strongly with the open metal sites of the magnesium oxide units in stages 1 and 2. The electron-density map of argon at 27 kPa (Fig. 3d) and corresponding electron density distribution profile (Fig. 3c) show two to three cylindrical layers of argon atoms adsorbed onto the walls (regime A in Fig. 1). This is followed by argon condensation in the pores, which commences at stage 3 and is accompanied by a steep increase in gas uptake (Fig. 3a, d). At roughly midway through stage 3, the corresponding  $hk = 10$  reflection intensity decreases sharply (Fig. 3b; Supplementary Fig. 10), while a new broad peak at  $q = 0.10 \text{ \AA}^{-1}$  emerges (marked by grey dashes in Fig. 4a)—evidence of collective adsorbate–adsorbate interactions. Although the pores are not yet completely filled, as indicated by the smeared-out electron density in the centre region of the pore (Fig. 3d), the emergence of this broad peak unambiguously represents an important point (termed the aggregation point) in the initiation of formation of extra adsorption domains, whereby adsorbate atoms gather in certain pore regions in higher numbers than the average.

The intensity of this broad peak reaches a maximum as stage 3 turns to stage 4 (33 kPa), and then decreases gradually to eventually disappear at the end of stage 4 (Fig. 4a). Furthermore, the density of argon in the centre region increases more than it does around the pore walls (Fig. 3d, stage 4) during both the appearance and the disappearance of the peak. The correspondence between the appearance/disappearance of this peak with the characteristics of the pore-filling process indicates that this unusual phenomenon originates from the complex collective behaviour of argon: argon atoms are not equally distributed throughout the available pores during stages 3 and 4 of the condensation process, but instead exhibit density fluctuations that result in extra adsorption domains with a higher-than-average argon concentration spanning several contiguous pores.

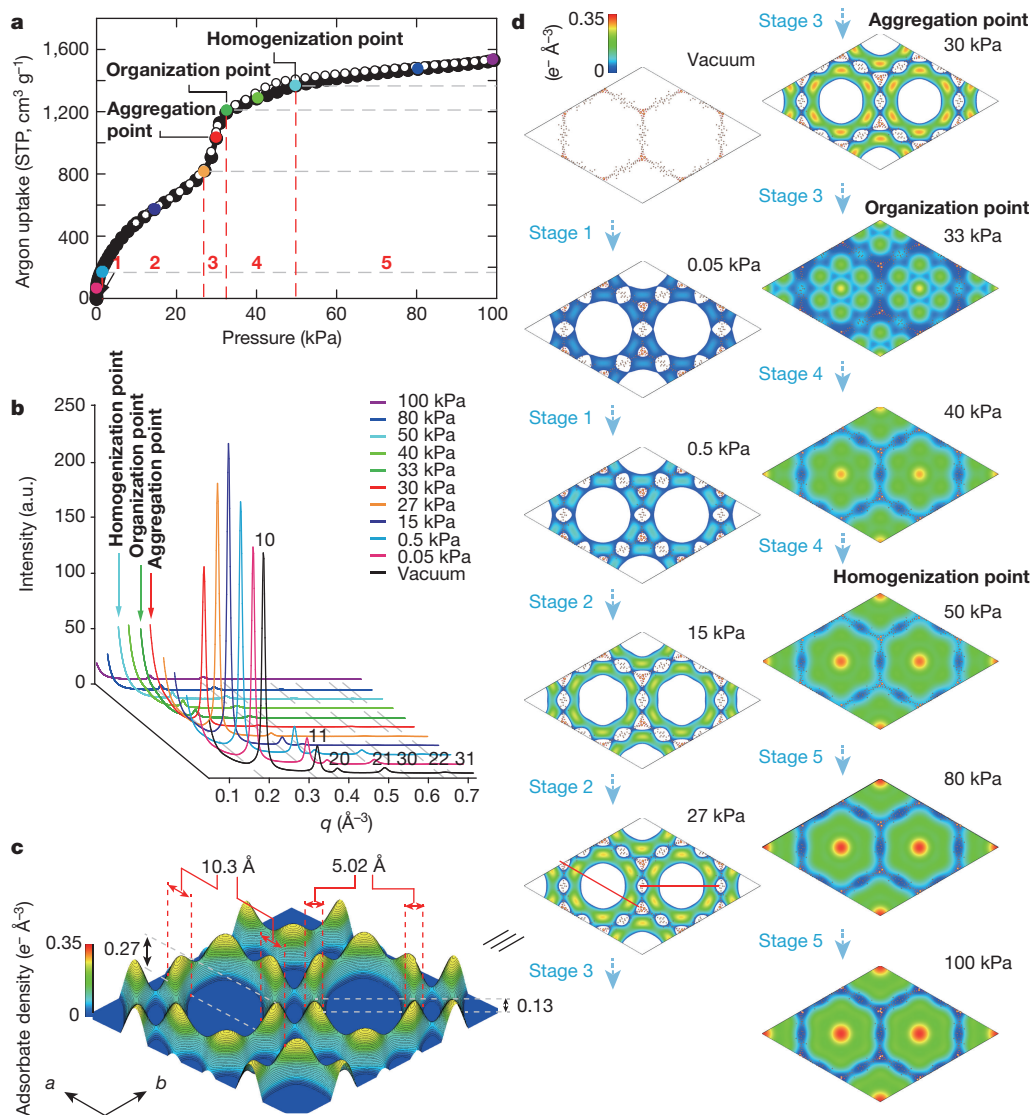


**Figure 3 | Mapping of argon distribution in IRMOF-74-V-hex.** **a**, Argon uptake by IRMOF-74-V-hex at different gas pressures. The isotherm shows five stages (1 to 5), with distinct slopes. Three points (red, dark green and light blue) are highlighted for the start, end/start and end of two events unobserved in type IV isotherms. **b**, SAXS scattering profiles measured along the entire adsorption process at 11 different gas pressures, covering the different stages of argon adsorption. The patterns are overlaid in linear scale, with colours corresponding to the points in the isotherm.

Further evidence for the formation of these domains comes from the adsorption profile slope in stage 4, which differs strongly from that in stage 3. The formation of the domains causes unit-cell contraction and associated broadening of the diffraction intensity profiles ( $hk = 10, 11, 20, 21, 30, 22$  and  $31$ ) during stage 3, and expansion of the unit cell and sharpening of the associated profiles during stage 4 (Fig. 4b–d). These effects are correlated with changes in the local strain of the MOF backbone, which results in the emergence of an additional stage in the overall adsorption process in IRMOF-74, as indicated by the full-width half-maxima (FWHM) of the SAXS profile peaks, and by the unit-cell parameters (contraction versus expansion) adopting during stage 3 maximum and minimum values, respectively (Fig. 4c, d). In stage 4, the strain induced by the adsorption heterogeneity starts to smear out and the FWHM decreases as more argon atoms enter the pores and move towards a more homogenized arrangement, leading to a different slope for gas uptake<sup>27</sup>. We note that the changes in the FWHM and unit-cell parameters of IRMOF-74 during and after mesopore condensation resemble those accompanying gas adsorption in MCM-41

(a typical mesoporous silica with relatively thick pore walls<sup>27</sup>), but the magnitude of the changes in our system is much larger than that observed for MCM-41. This indicates that the adsorbates stress the IRMOF-74 framework, with its thinner MOF walls, more than they stress the more-sturdy MCM-41 framework; this also explains why a broad peak at low  $q$  range and a unique slope at stage 4 could not be observed during and after mesopore condensation for MCM-41 (Supplementary Fig. 12).

The fate of the extra adsorption domains in IRMOF-74-V-hex can be gleaned from the abrupt appearance of superlattice reflections in the SAXS patterns (reflections at  $q = 0.25 \text{ \AA}^{-1}$  (marked by grey dashes) in Fig. 4a, and at  $q = 0.42 \text{ \AA}^{-1}$  in Supplementary Fig. 40) at the start of stage 4. The intensity of the reflections decreases as the pressure increases from 33 kPa, and becomes zero at 50 kPa (Fig. 4b), accompanied by a decrease in the FWHM of all the profile reflections. We infer from these observations that extra adsorption domains form, and that the contrast between these domains and the surrounding domains increases

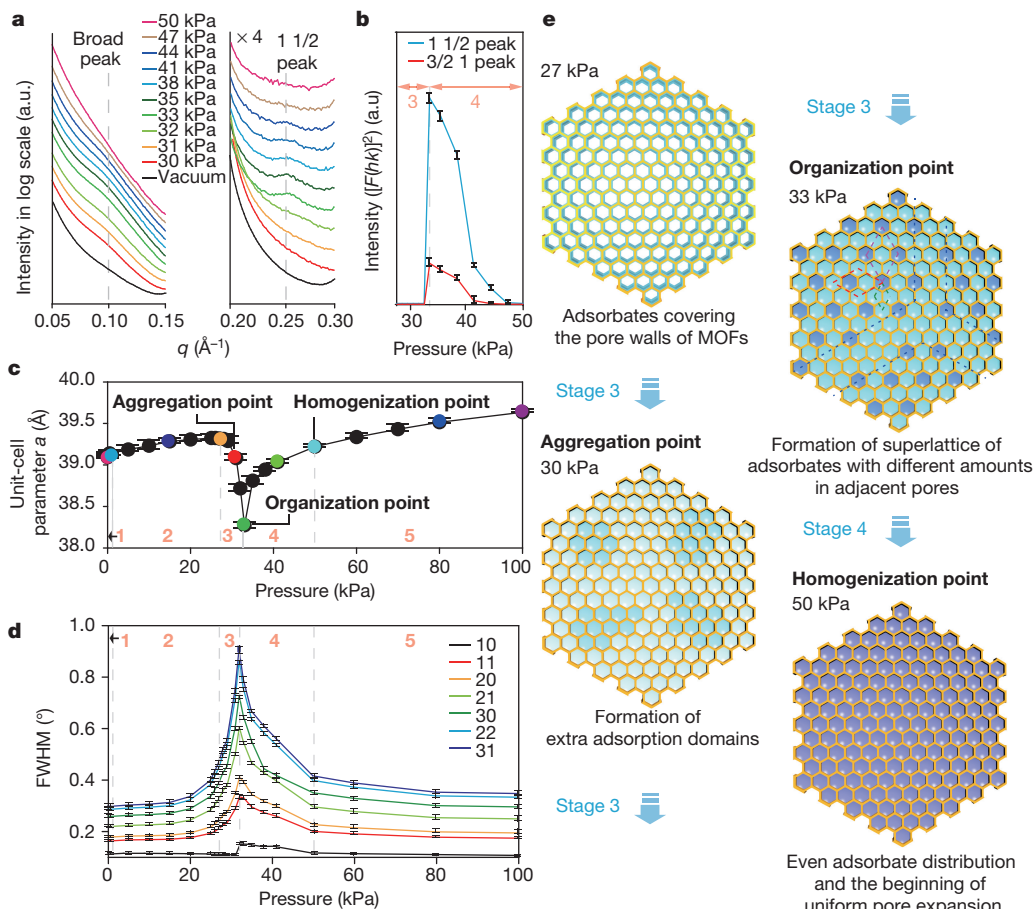


**Figure 4 | Extra adsorption domains and argon adsorbate superlattice in IRMOF-74-V-hex.** **a**, The appearance and disappearance of the broad peak (at  $q = 0.093 \text{ \AA}^{-1}$ ) and the superlattice peak (at  $q = 0.25 \text{ \AA}^{-1}$ ) in the SAXS patterns during the adsorption process, with intensity magnified by four in the right-hand image. **b**, Intensity changes of  $1\frac{1}{2}$  and  $\frac{3}{2}1$  superlattice reflections. **c**, Tracking of the unit-cell parameter change of IRMOF-74-V-hex during the adsorption process. **d**, Tracking of the corresponding FWHM

during stage 3 of the adsorption process (Supplementary Fig. 11); moreover, we conclude that once the point of maximum contrast (termed the organization point) has been reached, the domains commence to form the adsorbate superlattice in stage 4. It is the superlattice formation that relieves local strain—increasingly so as the contrast lessens and as more adsorbates fill the pores towards uniform distribution (Supplementary Fig. 11).

The precise structure of the superlattice is determined from the positions of the reflections at  $q = 0.25 \text{ \AA}^{-1}$  and  $q = 0.42 \text{ \AA}^{-1}$ , mentioned above, indexed by  $hk = 1\frac{1}{2}$  and  $\frac{3}{2}1$  and corresponding to an adsorbate superlattice structure with a  $2 \times 2$  unit cell (Fig. 2c, purple parallelogram, and Fig. 4e). Although this structure also gives a reflection of  $\frac{1}{2}0$  ( $q = 0.093 \text{ \AA}^{-1}$ ) that overlaps with the broad peak, the position and intensity of the two observed peaks rule out the possibility of a  $\sqrt{3} \times \sqrt{3}$  superlattice (Fig. 2b, red parallelogram, and Fig. 4e) that might form through modulation of the MOF structure. In such a case, the corresponding ordered reflection would have appeared at  $q = 0.29 \text{ \AA}^{-1}$  for  $hk = \frac{4}{3}\frac{1}{3}$ ; however, these were absent in the SAXS patterns. Note also that the line-widths of the adsorbate superlattice reflections are much larger than those of fundamental reflections, further suggesting that the origin of these extra peaks is not associated with the framework lattice. Detailed analysis of the FWHM revealed that the size of the superlattice domains is about  $400 \text{ \AA}$ .

Upon further increases in the argon pressure, the extra adsorption domains and superlattice reflections disappear at the end of stage 4 (Fig. 3a). During the next stage (stage 5), the adsorption isotherm

shows a new slope, and the electron density in the centre region of the pores gradually increases (Fig. 3d, stage 5) and leads to a slight unit-cell expansion (Fig. 4c) to accommodate more incoming argon atoms in a uniform manner among different pores. This changeover point in the isotherm (termed the homogenization point) marks the initiation of uniform pore expansion: the adsorbate superlattice disappears and homogenization of the adsorbate density takes place without involvement of the long-range adsorbate–adsorbate interactions that are mediated by local strain in the MOF framework. In terms of the amount of argon uptake, stages 4 and 5 account for up to 22% of the total uptake in IRMOF-74-V-hex.

of reflections in the SAXS profile. **e**, Illustration of the extra adsorption domains (aggregation point, 30 kPa) and superlattice (organization point, 33 kPa) formed as a result of argon being distributed unevenly among adjacent mesopores. Green, red and purple dashes indicate the original MOF,  $\sqrt{3} \times \sqrt{3}$ , and  $2 \times 2$  unit cell, respectively. The size of the argon superlattice domain (dark blue dashes at 33 kPa) is about  $400 \text{ \AA}$ .

An overview of how different SAXS characteristics document the different stages in the overall adsorption process is provided in Extended Data Fig. 1. The desorption process of argon in IRMOF-74-V-hex—which was also carefully studied (Fig. 3a) and compared with the adsorption process in detail (Supplementary Figs 7–9, Supplementary Tables 5 and 6, and Supplementary Video)—involves the same stages as those seen during adsorption.

The broad peak that is seen at low  $q$  values was observed in all IRMOFs for all three adsorbates studied (argon, nitrogen and carbon dioxide) (Supplementary Fig. 14). During stage 3, this peak was observed in the SAXS intensity profiles at  $q = 0.12 \text{ \AA}^{-1}$  and  $q = 0.094 \text{ \AA}^{-1}$  for IRMOF-74-IV and IRMOF-74-V, respectively. From the distance distribution function derived from the SAXS data in the  $q$  range of  $0.016 \text{ \AA}^{-1}$  to  $0.18 \text{ \AA}^{-1}$  for IRMOF-74-IV, and  $0.016 \text{ \AA}^{-1}$  to  $0.16 \text{ \AA}^{-1}$  for IRMOF-74-V and IRMOF-74-V-hex, the

maximum size of individual extra adsorption domains is calculated to be approximately 60 Å for IRMOF-74-IV, and 70 Å for IRMOF-74-V and IRMOF-74-V-hex. Although extra adsorption domains were seen in all IRMOF-74 compounds during the pore-filling process, the intensity of the additional reflections that are attributed to superlattice formation was negligible in the case of IRMOF-74-IV and IRMOF-74-V. The hexyl chains of IRMOF-74-V-hex thus seem to be important in superlattice formation, although pore size will also be relevant (as superlattices were not detected in IRMOF-74-VII, where hexyl chains are present but within the confines of larger pores).

The changes in the SAXS profiles seen during adsorption and desorption of all three adsorbates follow similar patterns (Supplementary Information, sections 2–5). Intriguingly, we also find that each of the three adsorbates desorbs at a different pressure, and that this adsorbate-specific desorption pressure is, to a first approximation, independent of the exact nature and pore size of the IRMOFs tested (Supplementary Tables 5, 9 and 11). This observation is another clear piece of evidence that adsorbate–adsorbate interactions within and across adjacent pores play a major role in gas uptake and release, both at the outset of the desorption process and in the formation of extra adsorption domains.

**Online Content** Methods, along with any additional Extended Data display items and Source Data, are available in the online version of the paper; references unique to these sections appear only in the online paper.

**Received 22 June 2014; accepted 8 September 2015.**

**Published online 9 November 2015; corrected online 25 November 2015**

**(see full-text HTML version for details).**

- Kitagawa, S., Kitaura, R. & Noro, S. Functional porous coordination polymers. *Angew. Chem. Int. Edn* **43**, 2334–2375 (2004).
- Furukawa, H., Cordova, K. E., O’Keeffe, M. & Yaghi, O. M. The chemistry and applications of metal-organic frameworks. *Science* **341**, 1230444 (2013).
- Rosi, N. L. *et al.* Hydrogen storage in microporous metal-organic frameworks. *Science* **300**, 1127–1129 (2003).
- Dincă, M. *et al.* Hydrogen storage in a microporous metal-organic framework with exposed Mn<sup>2+</sup> coordination sites. *J. Am. Chem. Soc.* **128**, 16876–16883 (2006).
- Farha, O. K. *et al.* *De novo* synthesis of a metal-organic framework material featuring ultrahigh surface area and gas storage capacities. *Nature Chem.* **2**, 944–948 (2010).
- Holst, J. R. & Cooper, A. I. Ultrahigh surface area in porous solids. *Adv. Mater.* **22**, 5212–5216 (2010).
- Makal, T. A., Li, J., Lu, W. & Zhou, H. Methane storage in advanced porous materials. *Chem. Soc. Rev.* **41**, 7761–7779 (2012).
- Deng, H. *et al.* Large-pore apertures in a series of metal-organic frameworks. *Science* **336**, 1018–1023 (2012).
- Nugent, P. *et al.* Porous materials with optimal adsorption thermodynamics and kinetics for CO<sub>2</sub> separation. *Nature* **495**, 80–84 (2013).
- Rowell, J. L. C., Spenser, E. C., Eckert, J., Howard, J. A. K. & Yaghi, O. M. Gas adsorption sites in a large-pore metal-organic framework. *Science* **309**, 1350–1354 (2005).
- Vaidyanathan, R. *et al.* Direct observation and quantification of CO<sub>2</sub> binding within an amine-functionalized nanoporous solid. *Science* **330**, 650–653 (2010).
- Yang, S. *et al.* Selectivity and direct visualization of carbon dioxide and sulfur dioxide in a decorated porous host. *Nature Chem.* **4**, 887–894 (2012).
- Serre, C. *et al.* Role of solvent-host interactions that lead to very large swelling of hybrid frameworks. *Science* **315**, 1828–1831 (2007).
- Rabone, J. *et al.* An adaptable peptide-based porous material. *Science* **329**, 1053–1057 (2010).
- Scherb, C., Koehn, R. & Bein, T. Sorption behavior of an oriented surface-grown MOF-film studied by in situ X-ray diffraction. *J. Mater. Chem.* **20**, 3046–3051 (2010).
- Bureekaew, S. *et al.* Control of interpenetration for tuning structural flexibility impacts on sorption properties. *Angew. Chem. Int. Edn* **49**, 7660–7664 (2010).
- Sato, H. *et al.* Self-accelerating CO sorption in a soft nanoporous crystal. *Science* **343**, 167–170 (2014).
- Inagaki, S., Guan, S., Ohsuna, T. & Terasaki, O. An ordered mesoporous organosilica hybrid material with a crystal-like wall structure. *Nature* **416**, 304–307 (2002).
- Zhao, D. *et al.* Triblock copolymer syntheses of mesoporous silica with periodic 50 to 300 angstrom pores. *Science* **279**, 548–552 (1998).
- Joo, S. H. *et al.* Ordered nanoporous arrays of carbon supporting high dispersions of platinum nanoparticles. *Nature* **412**, 169–172 (2001).
- Muroyama, N. *et al.* Argon adsorption on MCM-41 mesoporous crystal studied by in situ synchrotron powder X-ray diffraction. *J. Phys. Chem. C* **112**, 10803–10813 (2008).
- Miyasaka, K., Neimark, A. V. & Terasaki, O. Density functional theory of in-situ synchrotron powder X-ray diffraction on mesoporous crystals: argon adsorption on MCM-41. *J. Phys. Chem. C* **113**, 791–794 (2009).
- Rosi, N. L. *et al.* Rod packings and metal-organic frameworks constructed from rod-shaped secondary building units. *J. Am. Chem. Soc.* **127**, 1504–1518 (2005).
- Dietzel, P. D. C., Blom, R. & Fjellvåg, H. Base-induced formation of two magnesium metal-organic framework compounds with a bifunctional tetraprotic ligand. *Eur. J. Inorg. Chem.* **2008**, 3624–3632 (2008).
- Lin, L. C. *et al.* Understanding CO<sub>2</sub> dynamics in metal-organic frameworks with open metal sites. *Angew. Chem. Int. Edn* **52**, 4410–4413 (2013).
- Bon, V. *et al.* In situ monitoring of structural changes during the adsorption on flexible porous coordination polymers by X-ray powder diffraction: instrumentation and experimental results. *Microporous Mesoporous Mater.* **188**, 190–195 (2014).
- Gor, G. Y. *et al.* Adsorption of n-pentane on mesoporous silica and adsorbent deformation. *Langmuir* **29**, 8601–8608 (2013).

**Supplementary Information** is available in the online version of the paper.

**Acknowledgements** The authors acknowledge K. Ito, K. Sasaki, M. Kuribayashi and N. Muroyama (Rigaku America and Japan) and K. Nakai (Japan Bel) for technical support; N. Fujita and T. Nishimatsu (Tohoku University, Japan), H. Furukawa and Y. Zhang (University of California at Berkeley, USA) for their input; and A. Sawada (Kyoto University, Japan) for advice in designing the gas cell. Financial support was provided by WCU/BK21+ (to H.S.C., K.M., J.K.K., O.M.Y. and O.T.); HIMC of Global Frontier Project (2013M3A6B1078884) funded by the Ministry of Science, ICT and Future Planning and Korea Center for Artificial Photosynthesis (to J.K.K.); Berzelii Centre EXSELENT on Porous Materials (to O.T.); and BASF (Ludwigshafen, Germany) (to O.M.Y.). H.D. and Z.D. were supported by the 1000 Talent Plan of China, National Natural Science Foundation of China (21471118) and National Key Basic Research Program of China (2014CB239203). A.V.N. acknowledges support from the NSF ERC ‘Structured Organic Particulate Systems’.

**Author Contributions** O.T., K.M. and J.K.K. designed and set up the experimental system. O.T. and O.M.Y. designed and led the project. H.S.C., K.M. and H.D. performed the SAXS experiments. H.D., Z.D. and M.C. prepared samples. A.V.N. contributed discussion of the gas adsorption–desorption process. H.D., H.S.C., J.K.K., O.M.Y. and O.T. prepared the first version of the manuscript and all authors contributed to the final version.

**Additional Information** Reprints and permissions information is available at [www.nature.com/reprints](http://www.nature.com/reprints). The authors declare no competing financial interests. Readers are welcome to comment on the online version of the paper. Correspondence and requests for materials should be addressed to O.M.Y. ([yaghi@berkeley.edu](mailto:yaghi@berkeley.edu)) or O. T. ([terasaki@kaist.ac.kr](mailto:terasaki@kaist.ac.kr)).

## METHODS

**Synthesis of IRMOF-74 series.** Organic linkers were synthesized as reported previously<sup>8</sup>. IRMOF-74 samples were synthesized by combining organic linkers with  $\text{Mg}(\text{NO}_3)_2$  in a solution of dimethylformamide, ethanol and water, and then heated in an oven at 120 °C for 24 hours<sup>8</sup>. Needle-shaped crystals clustered in spherical forms were obtained. These IRMOF-74 samples were evacuated after solvent exchange with methanol nine times in three consecutive days to remove guest molecules.

**In situ gas adsorption SAXS measurement.** The *in situ* SAXS measurements for Ar,  $\text{CO}_2$  and  $\text{N}_2$  adsorption by IRMOF-74s (III, IV, V, VII and V-hex) were performed using a SAXS instrument (BioSAXS-1000; Rigaku, USA) equipped with a rotating anode X-ray source (FR-E+ Super Bright; Rigaku, Japan) and a gas adsorption instrument (BELSORP-max) together with a specially designed cell on a cryostat (Bel, Japan). We incorporated a sample cell inside the SAXS instrument, with a small chamber connected to the gas adsorption instrument placed outside. In addition, we used a large area detector combined with copper *K* $\alpha$  radiation from a rotating-anode X-ray source to provide precise measurement of both the intensity and the position of the diffraction peaks within a wide  $q (= 4\pi\sin\theta/\lambda)$  range, from 0.01 to 0.71  $\text{\AA}^{-1}$ . Measurements were carried out with copper *K* $\alpha$  radiation in the transmission mode with Confocal Max Flux Mirror, a two-dimensional Kratky block and a Pilatus-type detector in the SAXS instrument. The powder samples were mounted in two places next to each other at the same adsorbate environmental condition: one was within the hollow part of the stainless steel rectangular plate covered by polyether ether ketone (PEEK) polymer films, in the X-ray path for diffraction; the other was for improving accuracy in measuring gas adsorption/desorption isotherms. The assembled samples were connected thermally to the temperature-controlling cryostat system, where the temperature is controlled within  $\pm 0.01$  K, and to the gas adsorption instrument. The position of the sample cell was adjusted to the X-ray pathway within the chamber of the SAXS instrument at low temperatures before starting to take measurements.

A known weight ( $\sim 0.03$  g) of the IRMOF-74-III, IRMOF-74-IV, IRMOF-74-V, IRMOF-74-VII and IRMOF-74-V-hex samples was mounted in the sample cell and activated at 373 K for 6 hours under vacuum ( $\sim 0.01$  Pa) to remove the guest molecules before a series of measurements was taken. Activation of the IRMOF-74s was confirmed by comparing the argon isotherm of these MOFs at 87 K and  $\text{CO}_2$  isotherm at 273 K with those of the activated sample measured on the traditional adsorption instrument (Supplementary Fig. 3). Gases (Ar,  $\text{N}_2$  or  $\text{CO}_2$ ) were introduced into the sample cell under measurement temperatures; the gas pressure was changed, and then maintained for 5 min after the system reached equilibrium (we judge the system to have reached equilibrium if the pressure fluctuation is less than 1 Pa for 5 min, which took roughly 30 min), for each measurement. The SAXS instrument was synchronized to the gas adsorption measurement and each SAXS pattern was collected at each equilibrium point of the sorption isotherms (the exposure time for each measurement was 30 minutes). There was no pressure change after the SAXS measurement, confirming that the sample with adsorbates in the sample cell was at equilibrium.

Before the actual adsorption/SAXS measurement started, gas adsorption without SAXS measurement was performed to confirm the adsorption curve

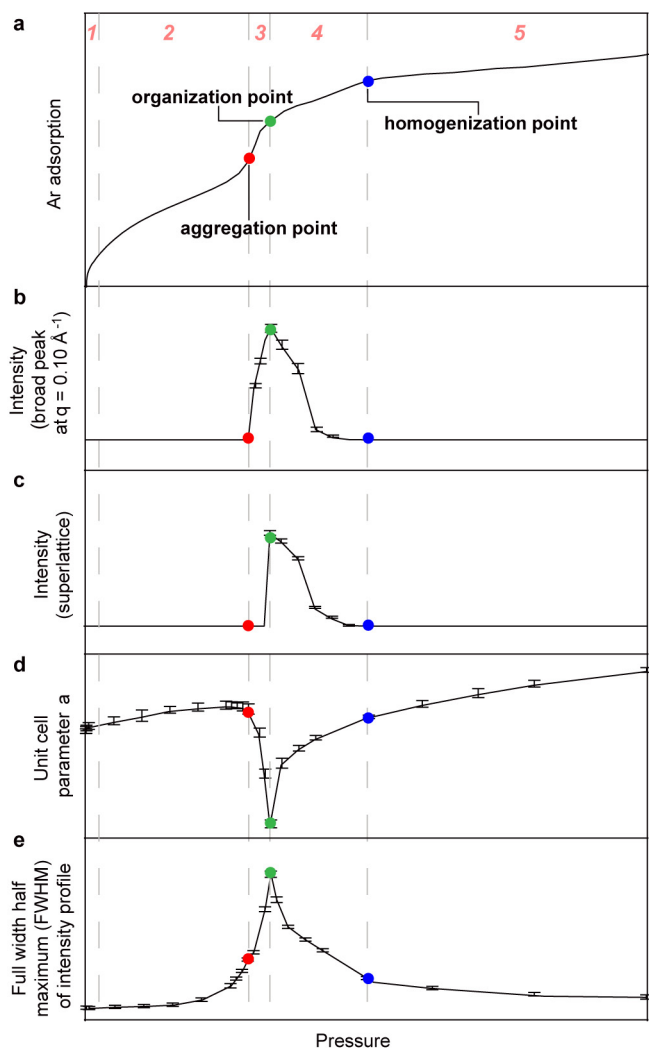
and to set up the SAXS measurement points. We then collected SAXS scattering profiles at each of the 24 equilibrium points in the adsorption process, including the initial point (in vacuum). Another 21 profiles were collected for the desorption process. No transformation in the structure of the backbone of IRMOF-74 occurred throughout the whole gas adsorption process, as confirmed by the absence of obvious changes in peak positions in these SAXS patterns. Moreover, the samples did not show structural differences after *in situ* gas adsorption SAXS measurement, confirmed by adsorption data and SAXS data in the vacuum.

**Structural analysis.** For the structural analysis of IRMOF-74s at different gas pressures, Le Bail refinements<sup>28</sup> were performed using the JANA program<sup>29</sup> over the full sampled angular range, on the basis of the space group *R*3 for IRMOF-74-IV, IRMOF-74-V and IRMOF-74-VII, and  $R\bar{3}$  for IRMOF-74-III and IRMOF-74-V-hex. The SAXS patterns of activated IRMOF-74 samples in the vacuum condition were refined first as a reference. The reflection peaks were modelled by a pseudo-Voigt peak-shape function modified for asymmetry, with six refinable coefficients. The background was treated using a Legendre polynomial with six refinable parameters. Because the  $q$  range for the SAXS instrument could cover only *hk0* reflections owing to the small unit-cell parameter  $c$ , only unit-cell parameter  $a$  was refined. The standard deviations of all data were derived from comparison of observed points in SAXS profiles with corresponding ones calculated after Le Bail refinement. The atomic coordinates for all MOF samples were adopted from the framework structures derived from single-crystal X-ray-diffraction data<sup>8</sup> (Supplementary Tables 1–4). Because the number of reflections is limited, framework atomic coordinates were fixed for all data with different gas pressures. The distribution of adsorbates was calculated by difference Fourier analysis between the observed intensity and calculated intensity after a careful check of phase relationships among different reflections, and visualized using the VESTA program<sup>30</sup>. The calculated intensity was derived from the atomic coordinates obtained from single-crystal X-ray-diffraction analysis of MOF structures and the atomic coordinates were fixed for different gas pressures. The correct phase relationship of the crystal-structure factors between different reflections was verified by the fact that we could observe electrons at the open metal sites at the beginning of gas uptake. Electron-density-map data were illustrated using  $\sqrt{3} \times \sqrt{3} p6$  cell, which is the hexagonal projected structure of  $R\bar{3}$  and *R*3, in order to show clearly the electron distribution in the pores (Fig. 1b, red parallelogram). The level of electron density ( $e^- \text{\AA}^{-3}$ ) is represented in blue/green/red colour code for all IRMOF-74 data. All electron-density-map data were presented with atomic coordinates of IRMOF-74 to clarify the relative position of adsorbates in the MOF.

28. Marra, G. L. *et al.* Cation location in dehydrated Na-Rb-Y zeolite: an XRD and IR study. *J. Phys. Chem. B* **101**, 10653–10660 (1997).

29. Petříček, V., Dušek, M. & Palatinus, L. Crystallographic computing system JANA2006: general features. *Zeitschrift Kristal. Crystalline Mater.* **229**, 345–352 (2006).

30. Momma, K. & Izumi, K. VESTA 3 for three-dimensional visualization of crystal, volumetric and morphology data. *J. Appl. Crystallogr.* **44**, 1272–1276 (2011).



**Extended Data Figure 1 | The five stages of gas adsorption in IRMOF-74s.** The five different adsorption stages are indicated in red at the top of the figure and their boundaries demarcated throughout all panels by grey dashed lines. **a**, The measured Ar adsorption by IRMOF-74-V-hex is shown; it can be compared against relevant SAXS profile features of IRMOF-74, measured as a function of Ar pressure, that are shown in the other panels. **b**, The appearance and disappearance of the broad peak indicates the formation of extra adsorption domains over pores (aggregation, red) and the even distribution of adsorbates (homogenization, blue). **c**, Intensity of  $1\frac{1}{2}$  superlattice reflection, appearing as stage 3 turns to stage 4 (organization, green) and disappearing at the end of stage 4 (homogenization, blue). **d**, Change in the unit-cell parameter  $a$  of IRMOF-74. **e**, Change in the line-profile width of IRMOF-74.